Finite element modelling of 3D printed continuous carbon fiber composites: embedded elements technique and experimental validation

A. Avanzini [a], D. Battini [a,*], L. Giorleo [a]

[a] *Department of Mechanical and Industrial Engineering, University of Brescia, Via Branze 38, I-25123 Brescia, Italy*

* *Corresponding author:* <u>davide.battini@unibs.it</u>   *Tel.: +39 030 3715807.*

ABSTRACT

A finite element approach for the simulation of composite parts with complex geometry realized by continuous fiber reinforced additive manufacturing is described. The embedded elements technique was adopted to accurately represent the layout of matrix and fibers while retaining an effortless finite element model setup. A simple specimen geometry with three different fiber layouts was chosen for experimental testing to allow the comparison of the embedded elements approach with conventional analytical or numerical methods for stiffness assessment. A complex specimen geometry with multiple notches was also printed, with three different fiber layouts, to further validate the use of the embedded elements technique in presence of 3D printed fiber deposition patterns for which conventional methods could not be applied. This study showed that the embedded elements approach, compared to more traditional techniques based on homogenization, may allow an accurate prediction of stiffness with the additional ability to model complex fiber deposition patterns, a simpler finite element analysis setup and a potentially richer output.

Keywords: Embedded elements; Reinforced composite; Continuous fiber; Finite elements; Mechanical Characterization; 3D printing

Glossary of acronyms

AM	Additive Manufacturing	FEA	Finite Element Analysis
CAD	Computer Aided Design	FEM	Finite Element Method
CAE	Complete Abaqus Environment	FFF	Fused Filament Fabrication
CFF	Continuous Filament Fabrication	MN	Multi-notch
CLPT	Classic Laminate Plate Theory	ROM	Rule of Mixture
EE	Embedded Elements	RP	Reference Points
FE	Finite Element	VAS	Volume Average Stiffness

1.   INTRODUCTION

Additive Manufacturing (AM) is an innovative approach to industrial production that facilitates the creation of ad hoc, lighter, and optimized components. Key advantages associated with AM are a greater freedom in design, with the possibility of creating complex geometries thanks to optimization algorithms (topology and generative design), and a

reduction of waste during production, as well as of the possibility to reduce the number of parts needed to create assemblies [1,2]. The materials suitable for AM production are many and heterogeneous and may be available in various formats: powders, filaments, chips, micro-spheres, liquid, etc. Materials for engineering applications include polymers, metals and ceramics [3,4], but the range is constantly evolving as a result of an increasingly specific demand for targeted applications. In the latest years, the production of composite materials realized through AM has made great steps forward, overcoming problems related to the limits of the printed part properties, the rate of production and printed part dimensions [5].

For composites, Fused Filament Fabrication (FFF) has evolved into Continuous Filament Fabrication (CFF) processes, which enable the reinforcement of complex parts with fibers in a more effective way in comparison with the conventional composite production methods [6]. While CFF reinforced parts can achieve similar (or higher) mechanical strength and stiffness compared to aluminum alloys, the development of a wider scientific knowledge in terms of mechanical behavior and numerical modelling is still necessary, due to the young age of the CFF technology. For example, the properties of these new materials are difficult to predict because they depend on the arrangement and type of fibers, on the matrix material and on the production process [7]. In fact, due to their anisotropy and heterogeneity, a mechanical characterization of composite materials is not straightforward. Although there are no standard mechanical testing methods that are specific of CFF, ASTM D638 [8] and ASTM D3039/3039M [9] standards are commonly used for tensile testing as CFF materials tend to be associated to laminates, being produced with a succession of layers.

The range of properties reported in literature is wide because there is no standard composite specimen and parameters such as fiber quantity and orientation are freely adjustable. As an example, in [10], the elastic modulus E ranged from 7.6 to 51.7 GPa and the ultimate tensile strength (R_m) ranged from 96.6 to 436.7 MPa. In [11] the ranges were 2.1-23.7 GPa and 27.2-304.3 MPa respectively for E and R_m and in [12], 47.75 GPa and 684 MPa were reported for E and R_m. Considering the complexity of these materials and the high number of tunable process parameters, it is clear how a numerical approach could be very useful for design and optimization purposes, as well as to reduce the efforts associated with experimental characterizations.

From this point of view, the heterogeneous material resulting from embedding the fibers into the matrix is usually represented as a homogeneous orthotropic lamina. The elastic constants (i.e. Young's moduli, Shear moduli, Poisson's ratios) can be derived from micromechanical models, ranging from the simple Rule of Mixture (ROM) for the determination of E_1 or ν_{12}, to more sophisticated approaches to estimate matrix dominated properties, such as E_2 or G_{12}, or even the out-of-plane response [13]. Having determined the elastic properties of a single lamina, the behavior of a laminate can then be investigated using analytical approaches, such as the Classic Laminate Plate Theory (CLPT), or numerically. In this latter case, one can take advantage of the tools, available in most finite element method (FEM) codes, for the definition of orthotropic laminae and laminate layup basing on lamina properties and local coordinate systems to manage different fiber orientations.

For example, CLPT was used to predict in-plane mechanical properties of continuous carbon fiber composites in [14], while the elastic properties of fiber reinforced 3D printed specimens were predicted using Volume Average Stiffness (VAS) method in [15]. This latter method uses micromechanical models to determine the effective properties of each single FFF-printed component. Subsequently, a coordinate system transformation is applied to the solid and infill layers and volume averaging of the stiffness matrices of each of the cross-sectional regions is performed. Micromechanical models can include specific features associated with FFF, such as porosities or different infill percentages, by treating the layers as plastic/void composites, as proposed in [16]. An analytical model based on VAS was also used in [17] to

predict elastic properties of 3D printed coupons. In [18] elastic properties were predicted as a function of volume fraction V_f by fitting experimental data and using the ROM.

Considering numerical analysis, finite element (FE) models with layered shell elements and homogeneous orthotropic lamina properties were adopted in [19] for tensile loading, in [20] to model three-point bending, and in [12] to simulate tests on coupons with open-hole configurations. Similarly, in [16] a finite element analysis (FEA) was developed using shell elements with composite lay-up, but in association with Hashin's damage initiation model to predict failure.

In general, it can be concluded that conventional modelling approaches based on homogenization were successfully applied for the simulation of the mechanical response of coupons for testing. Usually, these specimens exhibit a straight geometry with a fiber distribution similar to traditional composites, at least in the gage region, where fibers are uniformly aligned along the specimen axis (or at an angle).

However, these approaches may not be entirely consistent with the way 3D printed composites parts are manufactured, especially when fibers are laid with different intricate patterns within each layer. In particular, the additive manufacturing technologies allow the fiber to closely follow local changes in curvatures or paths designed according to topology optimization [21–23]. Moreover, due to manufacturing constraints or strategies, fibers may also follow specific patterns (i.e. isotropic/concentric) or only be placed in selected regions of the layer, differently from conventional composites in which all the fibers within a layer are usually uniformly distributed and aligned in the same direction. Consequently, as schematically shown in Fig. 1, when dealing with components including holes, notches or region with high curvature, the fiber paths for 3D printed composites can be quite different from those obtained with processes based on laminations of unidirectional layers or fabrics.
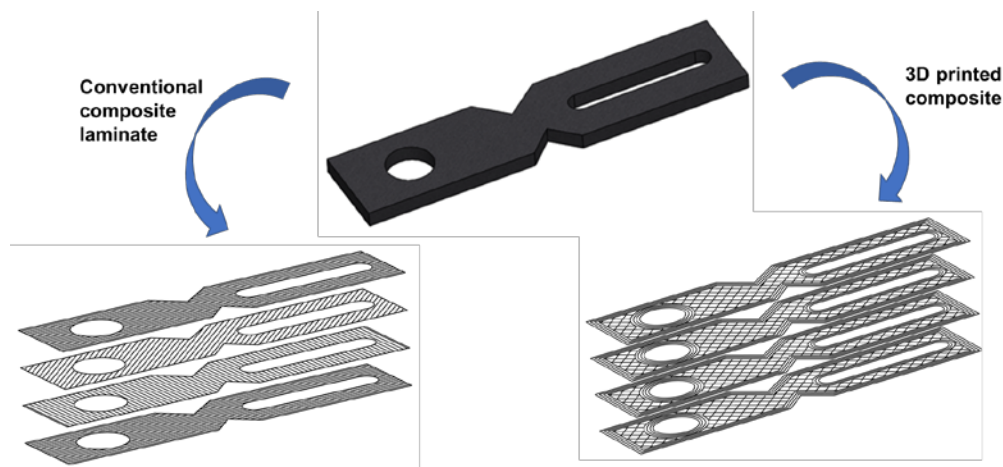
Fig. 1 – Schematic of a possible layer sequences on a generic representative geometry: conventional laminate vs. 3D printed composite.

In this case, modelling the layer as a homogeneous orthotropic material may be not sufficiently accurate or even hardly feasible. In fact, the geometry should be partitioned into a high number of discrete subregions, each with different homogenized properties, depending on the local presence, number and orientation of the fibers in each layer. This could prove being extremely challenging when the stacking sequence consists of different types of layer.

A possible approach to manage these issues is reported in [24], where an automated modeling system that creates elements based on the orientation of the fiber, obtained from image processing of the printing pattern, was implemented. Having defined, element by element, local orientations, two different sets of material properties were introduced to distinguish matrix (isotropic) and fiber reinforced regions (orthotropic). In [25] instead, fibers were simulated as a bundle with the width of 0.2 mm. To manage deposition of the fibers along curved trajectories,

corresponding to expected maximum or middle principal stress, fibers and matrix were defined separately as different isotropic materials, although no details on how this was implemented in the FEM code were provided.

In general, direct approaches in which matrix and fibers are represented as separate bodies, are difficult to apply to the case of full-scale components, because of the computational cost and the complexity of model set-up when dealing with bundles of small diameter fibers.

In this context, Embedded Elements (EE), a special finite element technique available in the commercial FEM software Abaqus [26], could provide an alternative and efficient solution, since this allows modelling the reinforcing fibers separately from the matrix in which they are enclosed and it is potentially applicable even for three-dimensional fiber patterns (not laying on a plane). In particular, the EE technique can be used to specify that an element or group of elements is embedded within its "host" elements. Basically, if an embedded node lies within a host element, the translational degrees of freedom at the node are eliminated and its translational degrees of freedom are constrained to the interpolated values (of the corresponding degrees of freedom) of the host element by means of weight functions [27]. Thus, when using the EE technique, the host (i.e. the matrix) and embedded parts (i.e. the reinforcing elements) can be meshed separately and independently, with solid or beam/truss elements respectively. Considering 3D printed composites, this allows creating complex reinforcement architectures as sequences of individual layers, each with its own specific spatial arrangement, while keeping the meshing of the matrix relatively simple. In the past, this method has been used to model the behavior of beams made of reinforced concrete [28,29], or of representative unit volumes (RVE) in the context of homogenization models of composite materials with complex architecture [30,31], or random short fibers [32–34].

In the present work, we tested the hypothesis that, for CFF composites, the EE technique could provide a good trade-off between the need to accurately reproduce fiber deposition pattern and that of keeping reasonably low the computational cost and the time for model preparation. To this aim, we investigated the application of the method to 3D printed composites obtained with a Markforged Mark Two™ printer, defining a specific workflow for the setup of a model starting from the real fiber deposition pattern layer-by-layer. At first, EE models were compared with experimental results on test coupons for which traditional modelling approaches could be applied. Then, EE models were also applied to more complex non-standard specimens, specifically designed to include complex geometric features and fiber paths that could not be modelled with homogenization techniques.

2. METHODS

2.1 Materials and specimens

All the specimens were produced with a Mark Two (Markforged – Massachusetts) FFF printer. Briefly, in the Markforged printing process a printing head with two separate extrusion nozzles for plastic and reinforcing fiber supply is adopted. The two nozzles do not work simultaneously and, unlike single nozzle systems, individual layers can be reinforced as described in [35]. Markforged printers employ a 0.4 mm filament diameter and can print with nylon, short carbon fiber–filled nylon, and a continuous fiber-filled nylon. The continuous fiber filament consists of several fibers bundled within a nylon matrix acting as a binder to allow for a correct interlayer and intralayer adhesion. The continuous fibers can be carbon, glass, or Kevlar [5] and are approximately 30–40 % volume fraction of the continuous fiber filament.

In the present work, specimen regions with a continuous fiber reinforcement were printed with a Markforged proprietary filament (usually referred as "carbon" in datasheets) consisting of several long carbon fibers embedded in a nylon matrix acting as binder. Specimen regions without continuous fiber reinforcement were instead printed with a

proprietary filament branded as Onyx™ consisting of a Nylon resin filled with micro-carbon fibers. While both filaments macroscopical mechanical properties are disclosed by Markforged, their exact composition and their constituent properties are not disclosed. For the above reasons, investigations on these filaments properties and composition were already carried out and reported in the current literature in [36–38] to which the present research refers. Onyx™ was printed at ≈ 270 °C and the continuous carbon fiber filament was printed at ≈ 240 °C.

The setup of the printing process parameters is controlled via a proprietary software (Eiger™). For unreinforced layers, these include infill percentage, wall count and number of top (also known as roof) or bottom (also known as floor) layers, whereas for reinforced layers the user can select fiber orientation, starting point for deposition and deposition strategy. Two deposition algorithms are available, namely isotropic and concentric. The first allows controlling fiber placement by the angle or by following inner and outer walls with concentric loops while the latter only allows for concentric loops but allows selecting which features to follow (i.e. internal and/or external walls). In presence of holes, notches, and curvatures these results in significantly different fiber patterns.

In order to investigate the applicability of the EE technique to the case of 3D printed composites, two different specimen geometries, identified as Rectangular (R) and Multi-Notch (MN) respectively, were designed for testing and modelling purposes.

The rectangular specimen geometry was used to compare EE both with experiments, with standard analytical approaches and numerical modelling techniques (i.e. orthotropic shell) for uniaxial tensile loading case. This geometry was designed according to ASTM 3039, opting for a rectangular shape because the use of CFF would cause a stress concentration along the curvature radius between the gripping section and the gauge [39] in the case of a dogbone shape. Specimens with different fiber volume fraction V_f and stacking sequences were obtained by changing the number of unreinforced layers (only placed at the top and the bottom) and the number and orientation of reinforced layers, so to investigate model predictions for different stiffnesses. All the rectangular specimens were 200 mm long and 15 mm wide. The number of walls was kept as low as possible which meant only a single wall was printed. The uniaxially reinforced specimens were designed to have the same eight unidirectional reinforced layers with fibers aligned with specimen length but a different number of roof and floor layers (unreinforced layers): R_uni_1-8-1 had one roof and one floor while R_uni_4-8-4 had four roof and four floor layers. The specimens R_qiso_4-8-4 included instead 8 reinforced layers with ±45°, 90° and 0°orientations with four roof and floor unreinforced layers, stacked to create a quasi-isotropic and symmetric composite. Table 1 shows a more detailed list of the main geometry and printing parameters for the rectangular specimens.

	R_uni_1-8-1	R_uni_4-8-4	R_qiso_4-8-4
Total Thickness [mm]	1.25	2	2
Width [mm]	15	15	15
Length [mm]	200	200	200
Nominal Layer thickness [mm]	0.125	0.125	0.125
Total Number of layers	10	16	16
Number of Roof/Floor layers	1/1	4/4	4/4
Matrix wire orientation [°]	+45/-45	+45/-45	+45/-45
Matrix layer infill	100%	100%	100%
Wall count	1	1	1
Number of reinforced layers	8	8	8
Reinforced layer positions (layer 1 = floor)	from 2 to 9	from 5 to 12	from 5 to 12
Fiber orientation in reinforced layers [°]	$[0]_8$	$[0]_8$	$[0/45/90/-45]_s$

Table 1: Design and printing features/parameters of the rectangular standard specimens.

The MN specimens, which purposely include several notches and curved regions, were used to investigate potential advantages and limitations of the application of EE to full scale parts, providing an example of a geometry for which

standard techniques based on homogenization were not applicable. The main dimensions and notch geometries are reported in Fig. 2. Each specimen consisted of a total of 40 layers and the wall count was increased to two as these specimens are bulkier. Their unreinforced layers were printed with the same infill, wire orientations and layer thickness of rectangular specimens (100%, +45°/-45°, 0.125 mm respectively).
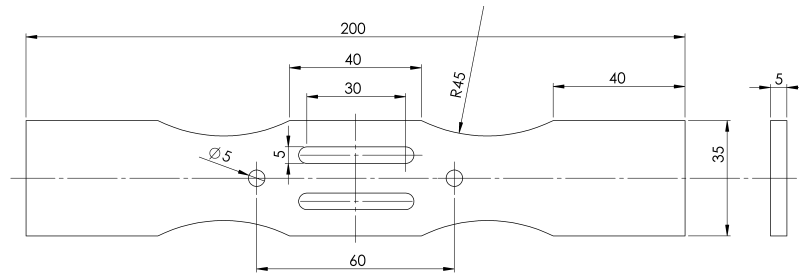

Fig. 2 – Multi-notch specimen geometry. All dimensions are reported in [mm].

For the MN geometry, three different combinations of fiber layup and path were created by using concentric deposition to place fibers along inner and/or outer curved walls or isotropic deposition to impose specific angles. For each specimen, the stacking sequence always included a total five groups of layers starting with an Onyx group and alternating with a continuously reinforced group. The different MN layups (see Fig. 3) were named respectively MN_iso (two isotropic fiber groups), MN_conc (two concentric fiber groups) and MN_mix (one isotropic fiber group from MN_iso and one concentric fiber group from MN_conc). Note that MN_mix has a non-symmetric stacking sequence.
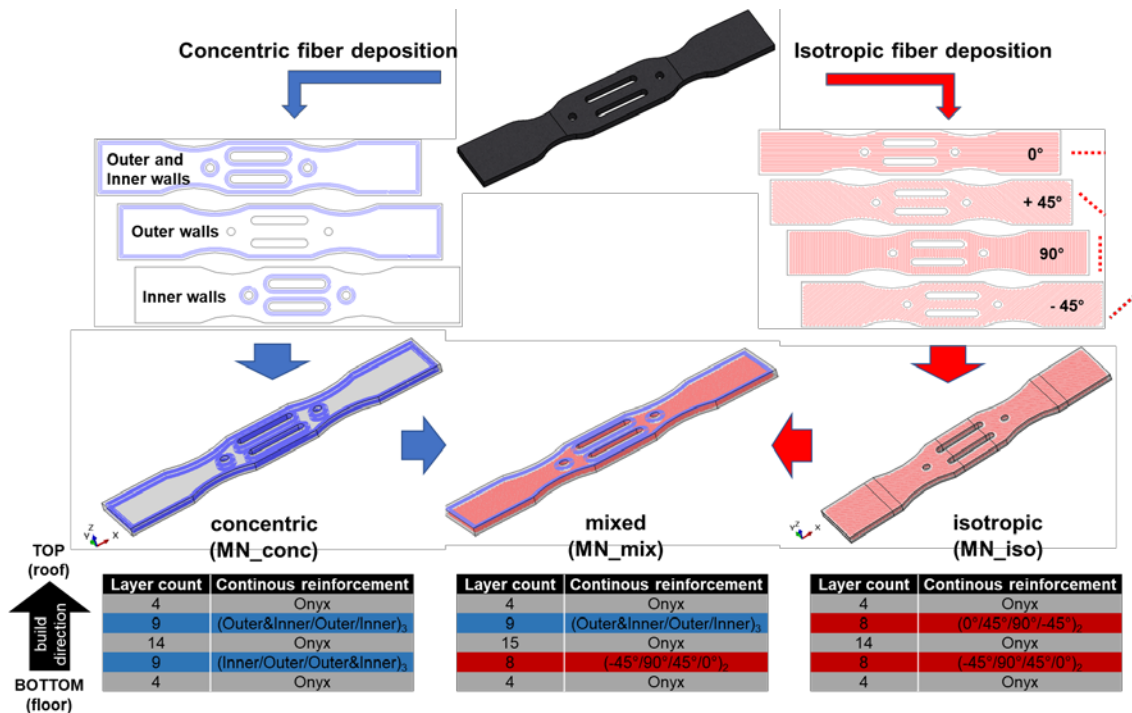

Fig. 3 – Multi-notch specimen fiber geometries and layer stacking sequences. Layer sequences for reinforced layers read up from left-to-right as top-to-bottom to allow for a top-to-bottom table reading.

Displacement controlled tensile tests for all the specimens were carried out on an Instron 8501 (100 kN max load) servohydraulic testing machine at a 0.5mm/min crosshead speed. No end tabs were applied on the coupons. An extensometer (Instron 2630-107, gage length of 25 mm) was used to have a more accurate deformation output. The sensor was mounted in the central region for the standard specimens and on the side of the central straight struts for the multi-notch specimens.

2.2 EE Model implementation

2.2.1 Workflow for set-up of EE model

Fig. 4 summarizes the workflow for setting up the EE model in Abaqus CAE (also known as Complete Abaqus Environment) which is the graphical user interface module provided within Abaqus software. However, this basic workflow is also valid for any FE software that supports EE. As a first step, embedded fibers and matrix (host) must be generated as separate parts. The geometric model of the matrix corresponds to that of the whole part, and it is usually straightforward to create it within a Computer Aided Design (CAD) environment. Considering fibers, the proprietary software Eiger™, which controls the printing process, allows visualization of each individual layer but not to export fiber architecture in a format directly usable in a CAE model. To overcome this difficulty, the following preliminary steps were required:

1. Acquisition of each different type of fiber layers as images (i.e. screenshots from Eiger™).
2. Import the fiber image in a CAD software and create corresponding layer as 2D part.
3. Export 3D fiber parts from a CAD in neutral format and import in CAE.
4. Create 3D fiber assembly in a CAE (or even directly in the CAD) software by placing the layers at the correct distance.
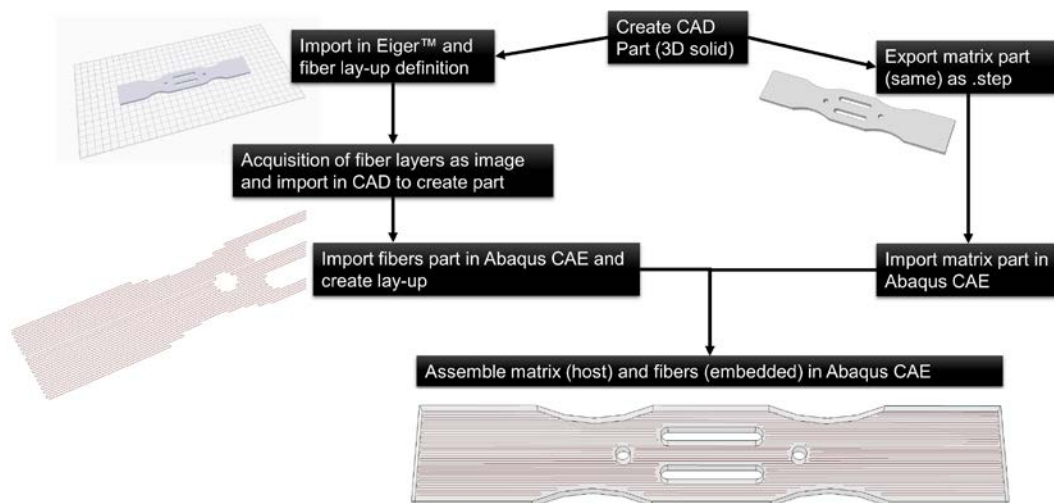

Fig. 4 – Workflow for model implementation of the embedded elements on a generic representative component.

Accordingly, 3D fibers and matrix were imported in Abaqus CAE as separate parts, so that each could be assigned different material properties and section/element types. Fibers and matrix were then assembled, and the embedding constraints were added by associating the host volume to the binder and the embedded volume to the fibers.

2.2.2 Matrix and fiber material models

When compared to the more classic and previously mentioned analytical approaches, a great advantage of the EE technique is that there is no need to calculate equivalent orthotropic properties for the reinforced layers. The properties of matrix, binder (host elements) and fibers (embedded elements) are instead required. First, area and profile to be associated with fiber cross-section must be defined. Markforged carbon filament, as schematically shown in Fig. 5, actually consists of several carbon fibers embedded in a nylon matrix that acts as binder [36]. According to literature, the diameter of the whole filament (before extrusion) is in the range 0.340-0.374 mm and its fiber volume fraction

(V_{f_fil}) is about 34.5% – 36.4% [10,14,40]. Basing on the estimated V_{f_fil} within the filament, one can determine the amount of carbon fiber that is being printed and its associated effective cross-sectional area. In fact, while modeling each single fiber is obviously unfeasible, fibers can collectively be represented as a single equivalent fiber with an effective area A_f calculated as per equation (1):

$$A_f = A_{fil}V_{f\_fil} \qquad (1)$$

where A_{fil} is the area of the ideal extruded filament section. As shown in Fig. 5, the filament is extruded into an approximately rectangular section with the same area, so one also has:

$$A_{fil} = b_{fil}h_{fil} \qquad (2)$$

Assuming a rectangular shape for the single equivalent fiber too, one can write

$$A_f = b_f h_f \qquad (3)$$

However, the dimensions b_f and h_f are somewhat arbitrary and we opted to determine these values from A_{fil} by maintaining the original form factor, i.e. by combining eq. (1), (2) and (3) into eq. (4) to equally rescale both the width and the thickness by the factor of $V_{f\_fil}^{0.5}$:

$$b_f h_f = A_f = A_{fil}V_{f\_fil} = b_{fil}h_{fil}V_{f\_fil} = \left(b_{fil}\sqrt{V_{f\_fil}}\right)\left(h_{fil}\sqrt{V_{f\_fil}}\right) \qquad (4)$$
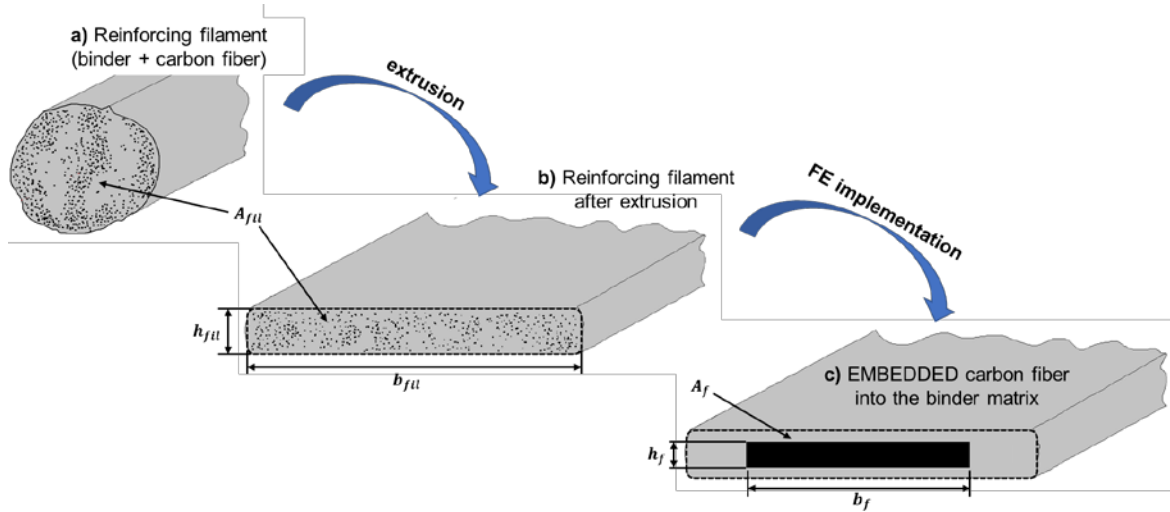

Fig. 5 – Continuous carbon fiber filament: raw 3D printed filament and idealization of the embedded element cross-section representing the extruded filament.

Following Markforged material datasheet, a filament diameter of ≈ 0.38 mm was assumed, resulting in A_{fil} equal to 0.1125 mm^2, b_{fil} equal to 0.9 mm and h_{fil} equal to the layer height (0.125 mm), from which the dimensions of equivalent fiber cross-section can be determined once V_{f_fil} is fixed. The extruded width, b_{fil}, of 0.9 mm was also corresponding to the fiber-to-fiber distance estimated from Eiger™ slicing images and resulted in a very reasonable 1:1 extrusion ratio. Within the FE model, the resulting profile section of A_f was then associated with the elastic modulus E_f of the "pure" carbon fiber. The mechanical properties of the fiber used by the Markforged printer have already been investigated in literature: Van der Klift [37] tested samples with fibers aligned unidirectionally and determined an elastic modulus $E_f =$ 231.4 GPa for a $V_{fil} = 34.5\%$ at filament level, a value that was subsequently assumed also in [24]. In [38], values of 191 GPa with $V_{f\_fil} = 36\%$ and 187 GPa with $V_{f\_fil} = 33.9\%$ were instead reported respectively for tests carried out after pyrolysis or acid digestion of polymeric matrix. Since these values are quite different, the choice of E_f and its associated cross-section dimensions and V_{f_fil}, may quite significantly affect model prediction. Therefore, the EE FE analyses were ran using two different data sets to define the linear elastic isotropic properties for the carbon fiber so that a range of

predictions could be identified. Specifically, following [38] and [37], a modulus of 191 MPa associated with a V_{f_fil} of 36% were used to catch a more compliant fiber behavior and a modulus of 231.4 GPa with a 34.5% V_{f_fil} were instead used to catch a stiffer fiber behavior. It is worth noting that carbon fibers may exhibit anisotropic properties. Since properties of the Markforged carbon fiber in the transverse direction are difficult to determine and were not reported in the above-mentioned studies, their values were assumed from the work of [30].

For the host matrix and unreinforced layers, a linear elastic isotropic behavior was also assumed. Following [38], the Onyx used for unreinforced layers matrix was given a value of E_{m1} = 1200 MPa, whereas for the matrix binder surrounding the fibers a value of E_{m2} = 800 MPa was used.

2.2.3   Simulation of tensile tests with EE

Tensile tests on rectangular and multi-notch specimens were virtually replicated using FEM software Abaqus by Dassault Systèmes.

In order to correctly simulate load application and boundary conditions, the specimens were partitioned, creating two side regions, with length corresponding to clamped area, and a tie constraint to reference points (RP). One of the RP was fixed and the other was prescribed the same translation as per experimental data, measuring the reaction force (or vice versa). In the central region a further partition was introduced by adding two measuring points with an initial distance equal to that between extensometer blades. This setup allows the definition of a virtual extensometer and an easy and consistent comparison of every quantity with experimental findings. Fig. 6 shows the boundary conditions and measuring points for the multi-notch specimen only as the same boundaries and measuring points are also used for rectangular specimens.
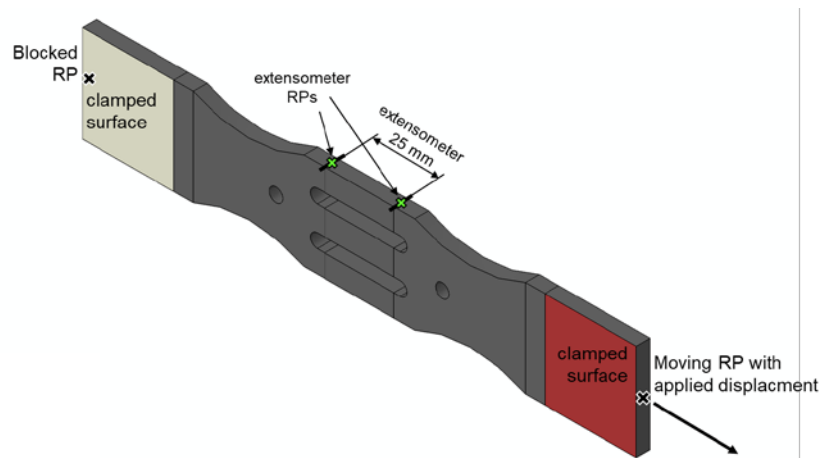
Fig. 6 – Multi-notch specimen with the applied boundary conditions and measuring points.

As shown in Fig. 7 for the multi-notch mixed configuration, the specimens were also partitioned along the thickness direction, to assign different properties to the unreinforced regions, and the embedding constraint was added.
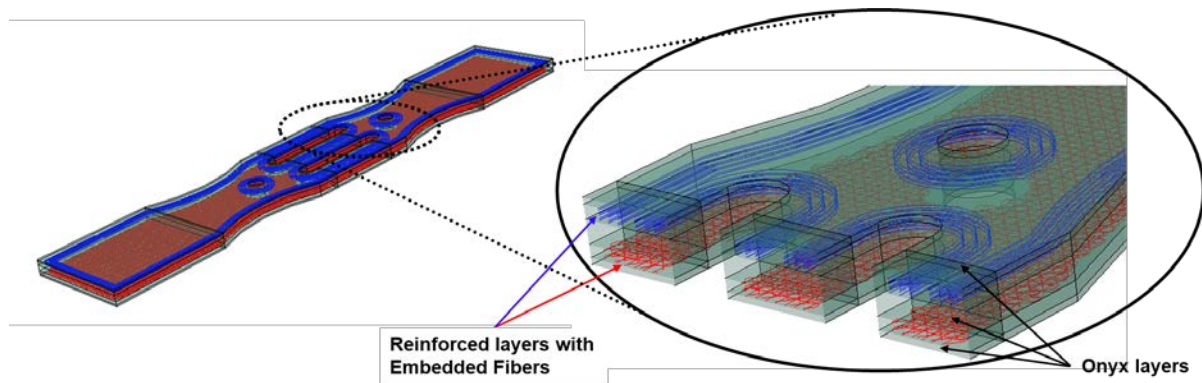
Fig. 7 – Example of a specimen partitioning and fiber embedding strategy (mixed configuration of the multi-notch specimen is shown).

The matrix was assigned second order solid elements with reduced integration (Abaqus label C3D20R) whereas for the fibers, second order beam elements (Abaqus label B32) were used.

The characteristic element lengths were set to 3÷6 mm for fiber elements and 1÷2 mm for matrix elements with possible smaller lengths over the thickness. As element lengths were kept similar, the number of elements ranged from less than 19000 ($\approx$ 14500 for the matrix and $\approx$ 4300 elements for the fibers) for the specimen R_uni_1-8-1 to $\approx$ 35000 for bigger specimens. A small mesh size sensitivity (at current size) was checked by running simulations with up to three times less and three times more elements for both the specimen geometries: stiffnesses, forces, displacements and stresses usually deviated of a few percent from the current results in the worst cases.

Non-linear geometries and materials were not considered as the current study is not aiming at an accurate description of the failure phenomena. For this reason, non-linearities caused by local damage effects (crack or matrix/fiber debonding) or macroscopic effects such as a visco-plastic response of the involved polymers were not included.

Overall, the computational cost of FE simulations was limited, and even the slower analyses required less than 5-10 minutes on a standard quad-core CPU with 32GB ram. Considering the limited computational cost, no backwards convergence study was performed to check the maximum element size granting sufficient accuracy for each specimen geometry and reinforcement configuration.

3. RESULTS AND DISCUSSION

3.1 Experimental tensile tests on standard specimens

In Fig. 8, the applied load is plotted against the displacement measured by the extensometer. The curves are almost linear until failure and a good repeatability is evident. The main results are summarized in Table 2, in which the subscript "*u*" stands for "ultimate" and denotes the failure condition.

As expected, the highest loads were sustained by unidirectional samples (R_uni_1-8-1, R_uni_4-8-4), for which failure occurred at similar level because they have the same reinforced layers. The quasi-isotropic specimens, R_qiso_4-8-4, failed at lower load levels because of the lower number of layers with 0° fiber orientation. Accordingly, the fact that quasi-isotropic specimens showed a more matrix dominated behavior also led to a slightly higher the elongation at break when compared to uniaxial specimens.
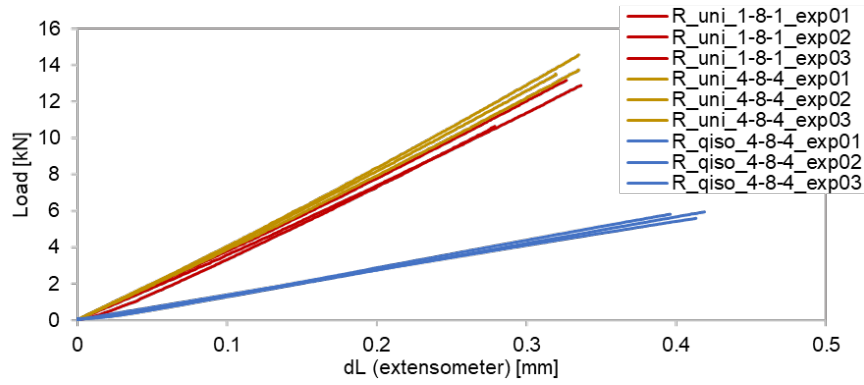
Fig. 8 – Experimental tensile tests for rectangular specimens shown as load-displacement curves.

Considering stiffness, the elastic modulus E_{exp} was calculated on the whole deformation range of the tests since, the high fiber content (compared to multi-notch specimens) led to a quite linear response during all test stages. Specifically, the maximum value of modulus E_{exp} was obtained with the specimen R_uni_1-8-1 due to the unidirectional reinforcement and higher V_f, whereas the most compliant response was observed for the quasi-isotropic specimen in which most of the fibers are not aligned with the loading direction. The noticeable difference in modulus for the two types of uniaxial specimens is due to their different thickness while having the same number of reinforced layers since the nominal stress was calculated as the ratio between the applied force and the nominal dimension of the specimen cross-section.

	R_uni_1-8-1 ($V_f = 25,4\%$)			R_uni_4-8-4 ($V_f = 15,6\%$)			R_qiso_4-8-4 ($V_f = 15,6\%$)		
	Test 1	Test 2	Test 3	Test 1	Test 2	Test 3	Test 1	Test 2	Test 3
F_u [kN]	10650	13160	12880	14580	13510	13740	5950	6050	5600
$\varDelta L_u$ [mm]	0.279	0.327	0.336	0.335	0.319	0.334	0.419	0.413	0.414
σ_u [MPa]	566	704	696	486	446	459	200	197	185
ε_u [mm/mm]	0.0111	0.0131	0.0135	0.0134	0.0128	0.0134	0.0167	0.0165	0.0165
E_{exp} [MPa]	52500	53700	51180	36200	35100	34170	12000	12200	11270

Table 2: Results of tensile tests on rectangular specimens. The elastic modulus and the ultimate (failure) quantities are reported for each test.

Interestingly, though not the primary aim of this work, different failure mechanisms were observed at final failure (see Fig. 9), including delamination processes and layer breakage, both close to the grips and in the central region of the specimen.
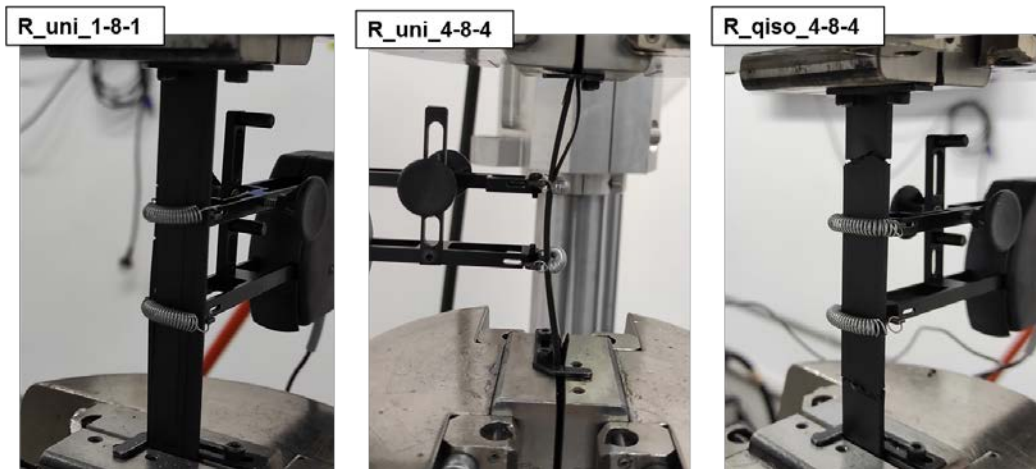

Fig. 9 – Failure of tensile tests on rectangular specimens. One specimen of each type is reported. From left to right: R_uni_1-8-1, R_uni_4-8-4 and R_qiso_4-8-4. Failure regions are highlighted with dotted red circles.

3.2 Simulation of tensile tests on standard specimens

As shown in Fig. 10, results of FE model with EE were compared with experimental data considering equivalent nominal stress-strain curves with the equivalent nominal stress being calculated as the ratio between applied force and nominal dimension of the specimen section and nominal strain as the displacement of extensometer points over their initial distance.

Fig. 10 and Table 3 also include numerical prediction using the FE model setup with composite shells instead of EE. The elastic properties of the homogeneous orthotropic lamina used in this latter model were calculated through classic micromechanical models from the average fiber and matrix properties used in the EE model. Average properties were used for the composite shell model instead of the full range used for the EE to simplify data visualization for Fig. 10. Similarly, Table 3 sums up all the elastic moduli by using average properties (in this case the average is also used for EE).

More specifically, the average value for E_f is 211200 MPa and the average V_f is 0.352 with the corresponding calculated homogeneous orthotropic lamina moduli being $E_1 = 67570$ MPa, $E_2 = 1200$ MPa, $G_{12} = 428$ MPa and $v_{12} = 0.33$. The out-of-plane shear moduli G_{13} and G_{23} were instead simply assumed equal to G_{12}. This assumption is confirmed by the lower and upper limits of the shear moduli that were recently identified for MarkForged carbon fiber composites in [41], where a range of 0.23-0.24 to 1.21-1.24 GPa was reported for G_{23} and a nearly coincident range of 0.24-0.26 to 1.44-1.51 GPa was reported for G_{12}. Nevertheless, a sensitivity analysis was run by assuming the extreme values and negligible effects were identified with output variations being always < 1%. While the determination of out-of-plane constants values was beyond our purposes, it should be remarked that for complex loading modes a more accurate determination could be necessary. The other elastic constants were also in good agreement with [41].

The shell model showed a good prediction of experimental results, and this was to be expected since matrix and reinforcement geometries are similar to those of classic laminate composites. A correspondingly good fit with experimental findings was also obtained with the EE models and both the EE and the shell models showed low deviation from experimental data for the whole strain range of the test since the linearity of experimental data was high from start to failure.
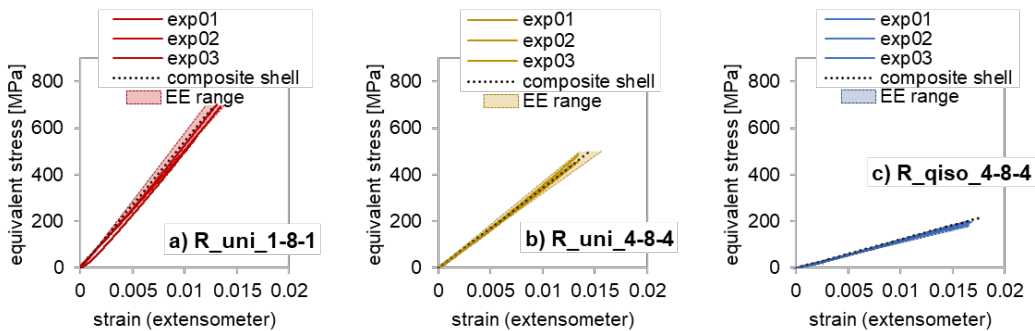

Fig. 10 – Tensile tests for (a) R_uni_1-8-1, (b) R_uni_4-8-4, (c) R_qiso_4-8-4. Finite element results are shown for the composite shell approach as black dotted lines and as range for the EE technique (due to the two different data sets used). Experimental curves are shown as continuous colored lines.

Finally, the apparent elastic modulus was also compared with analytical predictions using ROM (where applicable) and the classic method of effective constants calculated from ABD matrix as described in [13]. ROM was exclusively applied for specimens including layers with 0° orientation only (i.e. R_uni_1-8-1 and R_uni_4-8-4). The theoretical effective modulus E_{x_ROM} in the loading direction was obtained from the following equation:

$$E_{x_{ROM}} = E_f V_f + E_{binder} V_{binder} + E_{Onyx} V_{Onyx}$$

(5)

in which V_f, V_{binder} and V_{Onyx} are the volume fractions of the three constituents involved. These can be easily calculated from the geometry of the section, the number of reinforced and unreinforced layers and the number of reinforced filaments printed per layer, for which the actual amount of fiber is estimated basing on the fiber volume fraction in the filament, V_{f_fil}.

Alternatively, the effective (or apparent) elastic constants of a laminate E_{x_CLPT} can be calculated by treating the specimen as a laminate for which ABD matrix and its inverse can be calculated from the properties of the layers and their orientations. The method is also applicable to specimen R_qiso_4-8-4, which includes different orientations, and the elastic modulus in direction X can be calculated as:

$$E_{x_{CLPT}} = \frac{1}{tA'_{11}}$$

(6)

Where t is the thickness of the laminated specimen and A'_{11} is the first coefficient of the matrix A', obtained by inversion of ABD matrix. In order to determine the coefficients of ABD matrix, the reinforced layers were again considered as equivalent orthotropic laminae with the same elastic properties as in FE composite shell model.

All the different predictions (included EE) reported in Table 3 are carried out by considering intermediate values of E_f and V_f (i.e. $E_f = 211200$ MPa and $V_f = 0.3525$) to simplify data visualization.

	R_uni_1-8-1		R_uni_4-8-4		R_qiso_4-8-4	
	E [MPa]	error [%]	E [MPa]	error [%]	E [MPa]	error [%]
Experimental (average)	52460	-	35160	-	11820	-
FEM – Embedded Elements	54330	3.6	34410	-2.1	11710	-0.9
FEM – Composite shell	54290	3.5	34380	-2.2	12230	3.5
ROM	54300	3.5	34390	-2.2	-	-
Effective constants (CLPT)	54200	3.3	34330	-2.4	13780	16.6

Table 3: Comparison of experimental and predicted elastic moduli, E, of rectangular specimens. The reference modulus for error calculation is always the experimental modulus.

Clearly, for rectangular specimens the EE technique can be as effective as traditional numerical or analytical approaches in achieving a very good fit of test results. In addition, the FE EE model also allows highlighting the stress acting at fiber level separately from the matrix thus capturing both the global response and local stress gradients (see Fig. 11 for rectangular specimens stress maps). Remarkably, when the applied load reached the levels corresponding to experimental failure, the maximum principal stress in the fibers for all the specimens were in the range 3200 – 3600 MPa, which compares really favorably with the fiber strength of 3465 MPa reported in [37].

Overall, the application of EE technique could be considered validated against this set of experimental tests with standard geometries.
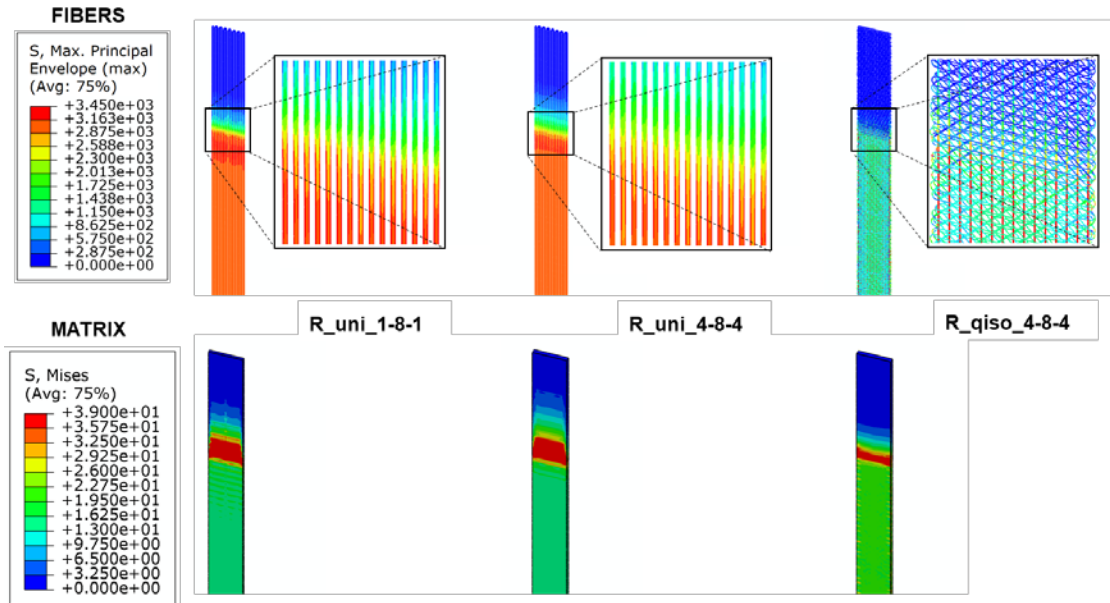
Fig. 11 – Maximum principal and Von Mises stress maps for embedded fibers and matrix respectively. Maps are taken from the stiffer fibers [37] simulation at the corresponding experimental failure displacement. From left to right: specimen R_uni_1-8-1, R_uni_4-8-4, R_qiso_4-8-4. Maximum legend values are failure stress for the carbon fibers [37] and yield stress [38] for the Onyx matrix.

3.3 Tensile tests on multi-notch specimen

Experimental data of tests on multi-notch specimens are presented in Fig. 12 in which the applied load is plotted as a function of the extensometer displacement. Among the three examined configurations, MN_iso was the stiffest (two isotropic fiber groups), MN_conc was the more compliant (two concentric fiber groups) and MN_mix featured an intermediate behavior (one isotropic fiber group from MN_iso and one custom concentric fiber group from MN_conc).
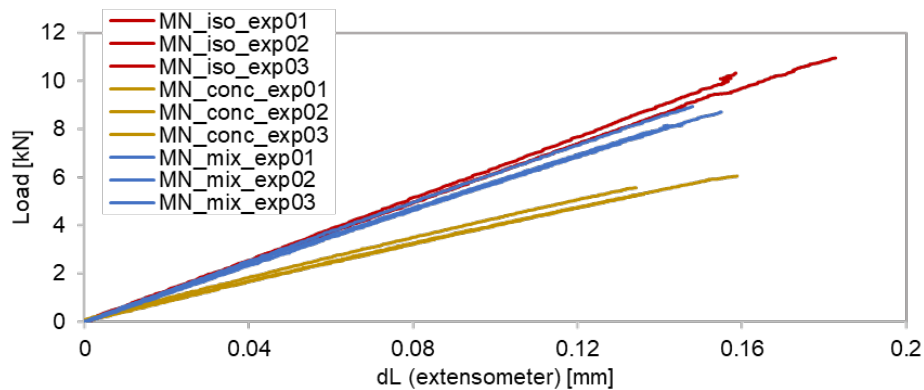

Fig. 12 – Experimental tensile tests for multi-notch specimens shown as load-displacement curves.

Considering failure, the specimens broke at different location, depending on the type of reinforcement, as shown in Fig. 13.
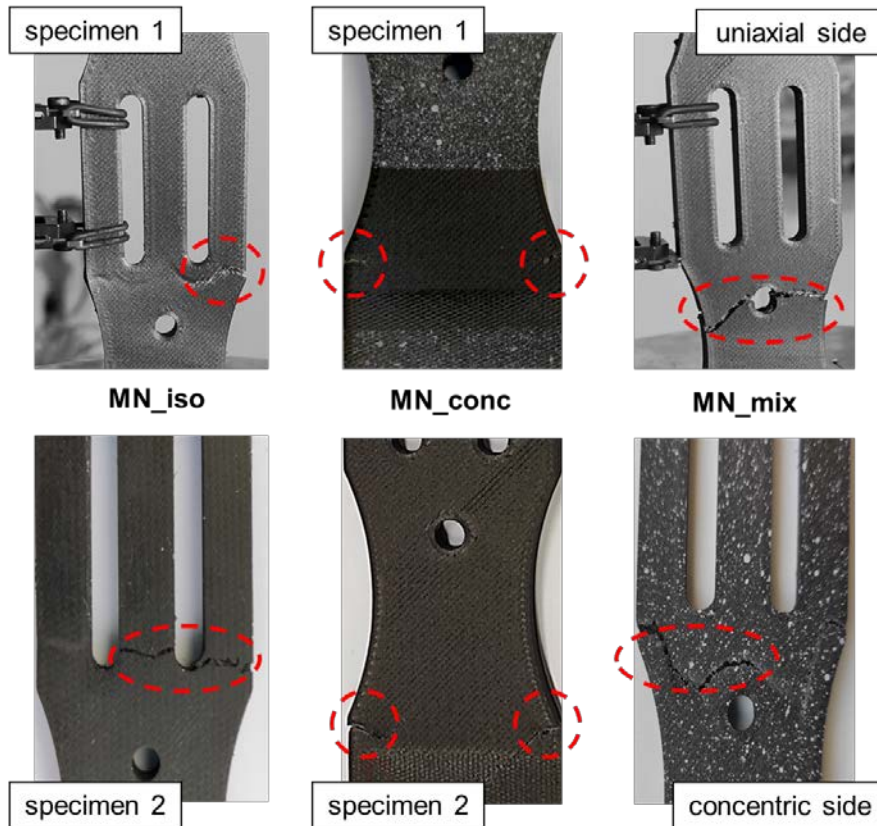
Fig. 13 – Failure regions of a tensile test. Specimens from left to right: MN_iso, MN_conc and MN_mix. Top and bottom images represent two different specimens for MN_iso and MN_conc and the two different sides of the same specimen for MN_mix. Failure regions are highlighted with dotted red circles.

For the isotropic configuration failure occurred for both specimens on the outer central strut, close to the end of the axial slot. Crack extended to the central strut in one case while followed the reinforcement contour close to the circular border in the other.

For the concentric specimens the failure occurred at the edge marking the transition between the clamping area (i.e. the straight and wide region at specimen end) and the section with a curved profile.

For the mixed specimen a more complex failure sequence was observed, possibly because of the asymmetric layer stacking sequence which introduced flexural effects caused by bending-extension coupling. Failure occurred on the net section across the small hole for the isotropic reinforcement side of the specimen, whereas on the opposite specimen side, the crack started from the outer edge, was then deflected by the concentric fibers around the curved profile and the hole until final failure was reached on the opposite side.

3.4   Simulation of tensile tests on multi-notch specimens with EE

In general, the EE model satisfactorily predicts the stiffness of the various specimens in the linear elastic regime even in presence of a complex geometry with notches and curvature variations. In particular the difference between concentric and isotropic deposition, as well as the intermediate response for the mixed configuration, were correctly identified. In this regards, equivalent stiffness values were calculated as the linear regression of the load signal over a predefined extensometer displacement range. In addition, stiffness was calculated on two different displacement ranges for experimental data: *exp_k@0mm*, is the stiffness calculated on the first 100 samples (with the extensometer reaching less than a 0.01 mm displacement) and *exp_k@0.1mm* is the value calculated on a 0.1 mm displacement range. Stiffness values are summed up in Fig. 14.

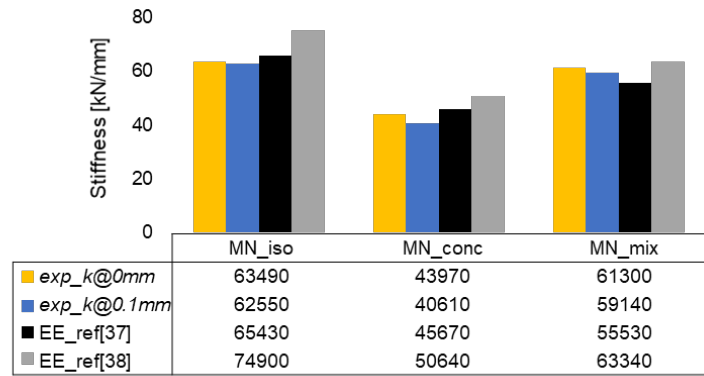|	MN_iso	MN_conc	MN_mix
exp_k@0mm	63490	43970	61300
exp_k@0.1mm	62550	40610	59140
EE_ref[37]	65430	45670	55530
EE_ref[38]	74900	50640	63340

Fig. 14 – Multi-notch specimens stiffness compared with the FE EE prediction range. Experimental stiffness is reported for both the initial value (exp_k@0mm) and the value calculated for at 0.1 mm extensometer displacement (exp_k@0.1mm).

A slight stiffness overestimation is evident in both Fig. 14 and Fig. 15 where the experimental load-displacement curves of MN specimens is plotted together with the FE EE range prediction to evaluate the effect of different assumptions of fiber properties and characteristics on non-trivial geometries.
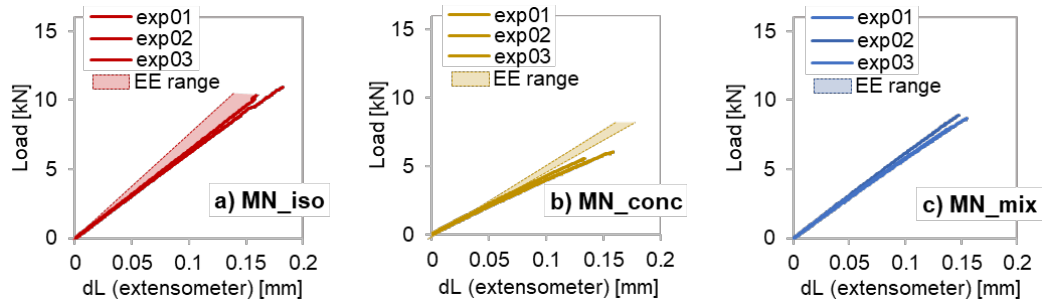

Fig. 15 – Tensile tests for multi-notch specimens: (a) MN_iso, (b) MN_conc, (c) MN_mix. EE Finite element results are shown as range (due to the two different data sets used) while experimental curves are shown as continuous colored lines. As calculating an equivalent nominal stress is not feasible due to specimen geometry, all data is represented as load-displacement curves.

This discrepancy is especially clear when compared to the predictions for the simple rectangular specimens previously reported. However, it is also evident this experimental dataset shows a stronger nonlinearity, which is particularly noticeable on MN_conc specimens. This nonlinearity can also be appreciated by looking at the stiffness reduction from the initial value *exp_k@0mm* to the value calculated on the wider displacement range, *exp_k@0.1mm*: MN_iso loses 1.5%, MN_conc 7.5% and MN_mix 3.5%.

In this perspective, stiffness prediction is in fact very good when directly comparing the compliant fiber FE EE simulations to the initial experimental stiffness *exp_k@0mm* (see again Fig. 14). Moreover, it should be noted that missing on nonlinearities is not a limitation of the EE model itself, but rather the obvious consequence of linear elasticity assumption for matrix and fibers. In fact, the same type of limitation would apply if more conventional approaches based on homogenized properties were attempted. More interestingly, this scenario suggests that it may be necessary to account for fiber damage and polymeric matrix nonlinear response, especially when the number of reinforced layers is limited (i.e. V_f is low) and fibers are not aligned with loading directions which is actually the case of a generic 3D printed composite. In addition, an accurate knowledge of constituent properties is paramount to achieve good accuracy.

On a side note, stiffness overestimation could also be regarded as something linked to a non-ideal microstructure of the specimens where voids could be present and deficient Onyx-binder bonding interactions could occur. Indeed, it is

reasonable to assume that such non-idealities would be more noticeable on massive specimens due to lower V_f and a wider Onyx-binder interface area. As for the nonlinear response, the same type of limitation would apply to more conventional approaches based on homogenized properties and it is EE-specific. If anything, the EE technique should facilitate the implementation of more complex modelling assumptions.

The failure locations can also be compared with maximum principal stress contour maps in the fiber architecture, as shown in Fig. 16 and Von Mises stresses in the matrix.
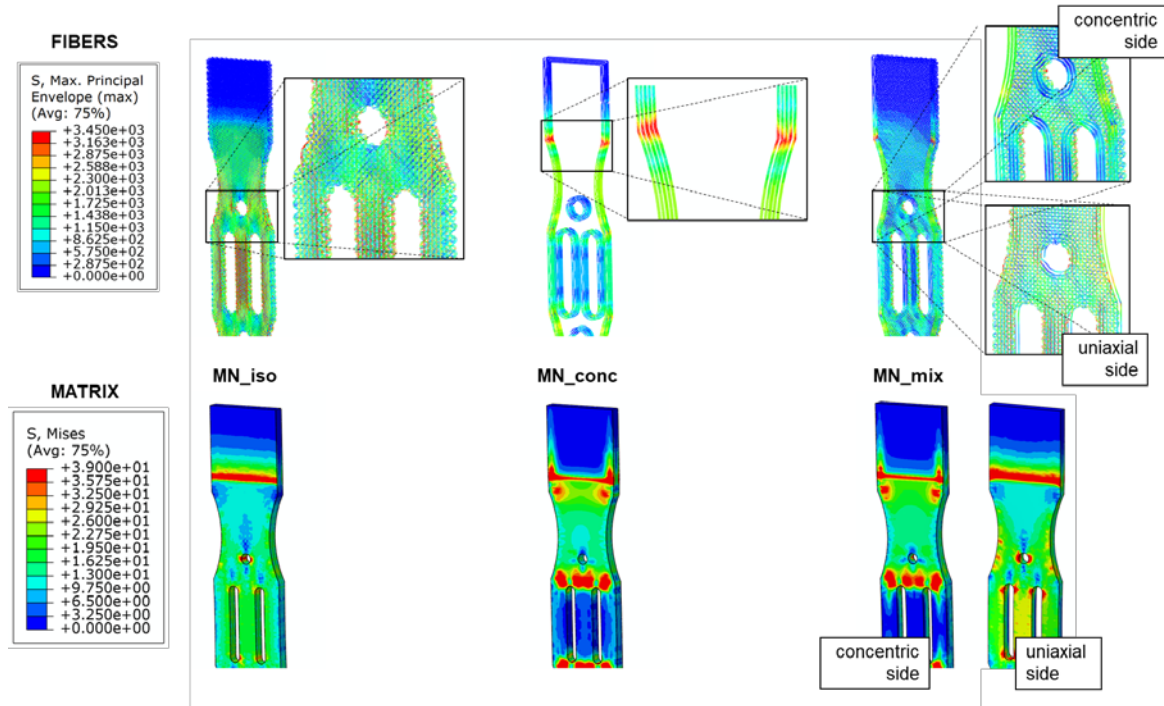

Fig. 16 – Maximum principal and Von Mises stress maps for embedded fibers and matrix respectively. Maps are taken from the stiffer fibers [37] simulation at the corresponding experimental failure displacement. From left to right: specimen MN_iso, MN_conc and MN_mix. Maximum legend values are failure stress for the carbon fibers [37] and yield stress [38] for the Onyx matrix.

Although no damage mechanism was implemented in the current FE analyses, matrix and fiber stress maps are still useful to check whether critical locations are predicted correctly or not. The stress range for Von Mises maps reported in Fig. 16 was fixed on a maximum value equal to the ultimate tensile stress from [37] for fibers and the yield stress from [38] for the matrix.

Regarding critical stress locations, the isotropic configuration (MN_iso) showed the peak fiber stress in the central region, within the central strut, in good agreement with the failure location observed experimentally (Fig. 13).

For the concentric configuration (MN_conc) the peak stress was also located in the same region where failure occurred: at the transition between straight and curved regions of the outer profile, showing how most of the load is borne by the fibers following the outer contour. When tensile load is applied these fibers get straightened and suffer higher stress levels, whereas the inner slots and hole are shielded.

For the mixed configuration the peak stresses were observed close to hole on the side of the specimen reinforced with the isotropic strategy, whereas the same location showed lower stress levels on the other side of the specimen. A similar behavior can also be observed on matrix stress maps. Interestingly, this peculiar stress distribution is well corroborated by the experimental failure: specimens failed in the same area, but crack followed different patterns on the two side of the specimens, as clearly shown in Fig. 13.

Finally, as shown Fig. 17, the EE model is also able to capture the characteristic bending-extension coupling determined by the asymmetry of the stacking sequence in the MN_mix configuration, further confirming the potential usefulness of the model.
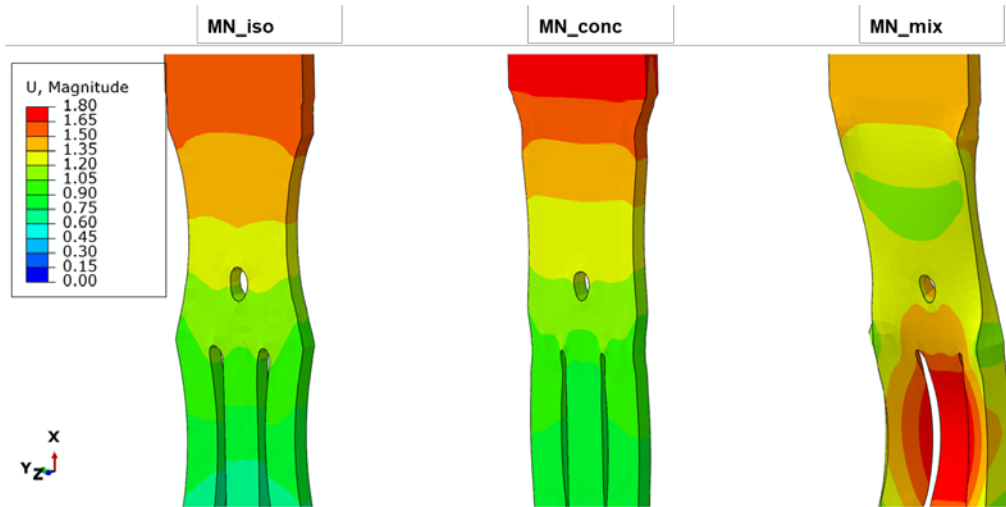

Fig. 17 – Displacement magnitude (in [mm]) maps with a 12x deformation scale factor to appreciate the huge differences in deformation modes due to the different reinforcement strategies. From left to right the specimens: MN_iso, MN_conc, MN_mix.

4.   PERSPECTIVE WORK AND LIMITATIONS

As discussed in the previous section, the results obtained with EE modelling technique are in good agreement with experimental findings for multi-notch and rectangular specimens. Of course, any model necessarily embodies simplifying assumptions and even for the EE modelling technique some limitations must be considered.

On the one hand, the EE model setup greatly simplifies materials definition with respect to other modelling approaches, as it is not required to calculate equivalent orthotropic properties nor to create local coordinate systems to manage material orientation, which could be extremely difficult dealing with complex lay-ups. On the other hand, the architecture of embedded fibers must be created, and this requires converting images from slicing software into 3D parts and then assembling the layers in the correct order and position in the host matrix volume. Since no direct export option is available in the closed-source Markforged software, some tedious manual work is therefore unavoidable. From this point of view, working with an open software or having the option to extract tool paths from Markforged software would allow a direct conversion of the sliced fiber patterns to a CAD part, greatly reducing the time needed to set up the model correctly. An alternative could also be the option of having a proper image-export feature in the Markforged software to build an automatic routine for the conversion of the fiber pattern image to a CAD part.

Additional possible issues with the embedded element technique can arise when volume redundancy is not negligible. In fact, with the EE approach the host matrix is usually a full solid, with no cavities or empty volumes at fiber locations, thus a 100% fiber-matrix superposition is present. This feature greatly simplifies the design and the discretization of the matrix while also avoiding the need contact interactions at matrix/fiber interfaces, however, the price to pay is that the redundant matrix volume contributes to the overall stiffness and density of the component. For the examined configurations, the high difference between the elastic modulus of the carbon fiber and the polymeric matrix, the relatively low V_f, and the quasi-static testing conditions, ensure that the additional stiffness and mass caused by matrix volume redundancy are negligible. In general, this volume redundancy can also be mitigated by compensating fiber properties for the added stiffness and mass, but careful considerations should always be carried out when compensation becomes necessary to achieve an otherwise insufficient accuracy.

In addition, care should be exerted when evaluating stresses at fiber level and predictions should be regarded as estimates since the single embedded fiber is not meant to represent each single fiber of the layer. Actually, when the filament is extruded the single fibers are displaced and distributed in the layer at different positions and height, as shown in [38][15]. Therefore, the predicted stress in the fiber is closer to the real ones especially when fibers are loaded along their axis and subject to membrane loading. The presence of high bending loads or extreme curvature changes of fiber paths may locally reduce accuracy. The choice of the profile shape associated with the embedded element is also somewhat arbitrary. Here we opted for a rectangular section to account, at least in an approximate way, for the fact that fibers after extrusion are spread over the layer, but different strategies could be used. In the author experience, for the present model using equivalent circular profiles or splitting the section into more sub-sections (i.e. three or five) did not change the model predictions.

An alternative approach could also be to consider the filament as a homogeneous fiber whose elastic modulus can be calculated using ROM. For example, by adopting values in [38], this would correspond to assume E = 69 GPa. In this case a rectangular profile can also be selected, but differently from the previous approach, the cross-section area of the profile associated to the embedded element should be equal to that of the whole filament (A_{fil}, or 0.9 mm wide and 0.125 mm thick in our case). This approach could bring the advantage of removing the need to model the binder material, effectively reducing model setup even more, while also giving a (probably) accurate bending response if fibers are distributed uniformly inside the extruded reinforcing filament. However, this is nonetheless a homogenization technique and thus brings some limitations such as the ideally unfeasible definition of a damage criteria since binder and fibers undergo much different damaging mechanisms.

Finally, by comparing experimental results and model predictions, some discrepancies could be noticed especially when experimental responses deviated from linearity. These aspects, clearly related to damage occurring in the fiber or in the matrix, were not captured by the present version of the model, in which both phases were considered as linear elastic. It should be noticed however, that splitting the modelling of the fiber and of the matrix opens to further opportunities from a constitutive modelling point of view. As an example, the next developments of the model could be to include elasto-plastic or visco-plastic response of the matrix and/or a damage model for the fibers. Assuming an isotropic nature of the matrix, robust models already in use could be adopted, without the need to adapt complex theories to the anisotropic nature of a composite material. Similarly, since delamination was observed as a possible failure mode, the possibility to apply cohesive elements technique could be explored as well as the application XFEM models to predict crack propagation.

In the end, while the simple rectangular specimen showed a better agreement in terms of FEM vs experimental data, a slight overestimation of stiffness could be identified for multi-notch specimens. This discrepancy can probably be regarded as a non-ideal microstructure where voids and imperfect bonding between reinforced layers and Onyx matrix could be present. In fact, it is reasonable to assume that these non-ideal features would be more influential on complex specimen due to higher Onyx presence, higher thickness and higher number of reinforced layers causing wider Onyx-binder interface areas. In this sense, besides the typical voids caused by the FFF process the presence of porosities could be also justified by the reinforcing filament dimensions. In fact, the ideal reinforced filament area after deposition should be 0.9 mm wide and 0.125 mm thick, corresponding to a filament diameter of ≈ 0.3785 mm (assuming a 1:1 length ratio justified by the presence of carbon fibers) but the current literature reports variations of measured diameter in the range of 0.340-0.374 mm [10,14,40].

5. CONCLUSIONS

Considering the comparison between experimental tests and FE analyses on rectangular coupons and multi-notch specimens, the following concluding remarks were identified:

- The proposed approach, centered on the use of embedded elements in a finite element environment to represent fiber reinforcement, can be as effective as traditional approaches, based on composite shells with homogenized orthotropic properties, when dealing with standard specimen configurations used for material characterization.

- In comparison with conventional methods, either analytical or numerical, EE FE provides the additional opportunity to model complex fiber deposition patterns common to 3D printing technologies, which could not otherwise be implemented with approaches based on homogenized equivalent properties.

- The EE FE model provided accurate estimates of the stiffness of the 3D composite even in presence of notches, curvatures or when combinations of concentric and isotropic deposition strategies were used. The setup of the model can be a bit tedious depending on the complexity of fiber layup, but this additional work is compensated by the straightforward definition of the constituents material properties.

- The current version of the model misses on capturing nonlinear responses, which could be relevant for some types of 3D printed composites, due to the linear elasticity assumption. On the other hand, independent constitutive modelling of fiber and matrix can open new possibilities to refine predictions when the behavior under highly non-linear conditions (i.e. at failure) is of interest.

Declarations of interest

We wish to confirm that there are no known conflicts of interest associated with this publication.

Data availability

The raw and the processed data required to reproduce these findings cannot be shared at this time as the data also forms part of an ongoing study.

Bibliography

[1]   Frazier WE. Metal Additive Manufacturing: A Review. J Mater Eng Perform 2014;23:1917–28. doi:10.1007/s11665-014-0958-z.

[2]   DebRoy T, Wei HL, Zuback JS, Mukherjee T, Elmer JW, Milewski JO, et al. Additive manufacturing of metallic components – Process, structure and properties. Prog Mater Sci 2018;92:112–224. doi:10.1016/j.pmatsci.2017.10.001.

[3]   Ngo TD, Kashani A, Imbalzano G, Nguyen KTQ, Hui D. Additive manufacturing (3D printing): A review of materials, methods, applications and challenges. Compos Part B Eng 2018;143:172–96. doi:10.1016/j.compositesb.2018.02.012.

[4]   Ligon SC, Liska R, Stampfl J, Gurr M, Mülhaupt R. Polymers for 3D Printing and Customized Additive

Manufacturing. Chem Rev 2017;117:10212–90. doi:10.1021/acs.chemrev.7b00074.

[5]   van de Werken N, Tekinalp H, Khanbolouki P, Ozcan S, Williams A, Tehrani M. Additively manufactured carbon fiber-reinforced composites: State of the art and perspective. Addit Manuf 2020;31:100962. doi:10.1016/j.addma.2019.100962.

[6]   Wang Y, Zhou Y, Lin L, Corker J, Fan M. Overview of 3D additive manufacturing (AM) and corresponding AM composites. Compos Part A Appl Sci Manuf 2020;139:106114. doi:10.1016/j.compositesa.2020.106114.

[7]   Guo N, Leu MC. Additive manufacturing: Technology, applications and research needs. Front Mech Eng 2013;8:215–43. doi:10.1007/s11465-013-0248-8.

[8]   ASTM D 638 - 02a. Standard Test Method for Tensile Properties of Plastics 2003;08.

[9]   ASTM-D3039/D3039 M -17, Standard Test Method for Tensile Properties of Polymer Matrix Composite Materials n.d.

[10]   Chacón JM, Caminero MA, Núñez PJ, García-Plaza E, García-Moreno I, Reverte JM. Additive manufacturing of continuous fibre reinforced thermoplastic composites using fused deposition modelling: Effect of process parameters on mechanical properties. Compos Sci Technol 2019;181:107688. doi:10.1016/j.compscitech.2019.107688.

[11]   Naranjo-Lozada J, Ahuett-Garza H, Orta-Castañón P, Verbeeten WMH, Sáiz-González D. Tensile properties and failure behavior of chopped and continuous carbon fiber composites produced by additive manufacturing. Addit Manuf 2019;26:227–41. doi:10.1016/j.addma.2018.12.020.

[12]   Pyl L, Kalteremidou KA, Van Hemelrijck D. Exploration of the design freedom of 3D printed continuous fibre-reinforced polymers in open-hole tensile strength tests. Compos Sci Technol 2019;171:135–51. doi:10.1016/j.compscitech.2018.12.021.

[13]   Jones RM. Mechanics of Composite Materials - 2nd edition, Taylor&Francis Ed. 1999. doi:10.1115/1.3423688.

[14]   Saeed K, McIlhagger A, Harkin-Jones E, Kelly J, Archer E. Predication of the in-plane mechanical properties of continuous carbon fibre reinforced 3D printed polymer composites using classical laminated-plate theory. Compos Struct 2021;259:113226. doi:10.1016/j.compstruct.2020.113226.

[15]   Melenka GW, Cheung BKO, Schofield JS, Dawson MR, Carey JP. Evaluation and prediction of the tensile properties of continuous fiber-reinforced 3D printed structures. Compos Struct 2016;153:866–75. doi:10.1016/j.compstruct.2016.07.018.

[16]   Rodríguez JF, Thomas JP, Renaud JE. Mechanical behavior of acrylonitrile butadiene styrene fused deposition materials modeling. Rapid Prototyp J 2003;9:219–30. doi:10.1108/13552540310489604.

[17]   Al Abadi H, Thai HT, Paton-Cole V, Patel VI. Elastic properties of 3D printed fibre-reinforced structures. Compos Struct 2018;193:8–18. doi:10.1016/j.compstruct.2018.03.051.

[18]   Hou Z, Tian X, Zheng Z, Zhang J, Zhe L, Li D, et al. A constitutive model for 3D printed continuous fiber reinforced composite structures with variable fiber content. Compos Part B Eng 2020;189:107893. doi:10.1016/j.compositesb.2020.107893.

[19]   Žmindák M, Novák P, Soukup J, Milosavljevic D, Kaco M. Finite element simulation of tensile test of composite materials manufactured by 3D printing. IOP Conf Ser Mater Sci Eng 2020;776. doi:10.1088/1757-899X/776/1/012082.

[20]   Ghebretinsae F, Mikkelsen O, Akessa AD. Strength analysis of 3D printed carbon fibre reinforced thermoplastic using experimental and numerical methods. IOP Conf Ser Mater Sci Eng 2019;700. doi:10.1088/1757-899X/700/1/012024.

[21] Li N, Link G, Wang T, Ramopoulos V, Neumaier D, Hofele J, et al. Path-designed 3D printing for topological optimized continuous carbon fibre reinforced composite structures. Compos Part B Eng 2020;182:107612. doi:10.1016/j.compositesb.2019.107612.

[22] Papapetrou VS, Patel C, Tamijani AY. Stiffness-based optimization framework for the topology and fiber paths of continuous fiber composites. Compos Part B Eng 2020;183:107681. doi:10.1016/j.compositesb.2019.107681.

[23] Esposito L, Cutolo A, Barile M, Lecce L, Mensitieri G, Sacco E, et al. Topology optimization-guided stiffening of composites realized through Automated Fiber Placement. Compos Part B Eng 2019;164:309–23. doi:10.1016/j.compositesb.2018.11.032.

[24] van de Werken N, Hurley J, Khanbolouki P, Sarvestani AN, Tamijani AY, Tehrani M. Design considerations and modeling of fiber reinforced 3D printed parts. Compos Part B Eng 2019;160:684–92. doi:10.1016/j.compositesb.2018.12.094.

[25] Zhang H, Yang D, Sheng Y. Performance-driven 3D printing of continuous curved carbon fibre reinforced polymer composites: A preliminary numerical study. Compos Part B Eng 2018;151:256–64. doi:10.1016/j.compositesb.2018.06.017.

[26] ABAQUS CAE User's Guide - Embedded Elements, Dassault-Systemes (1995-2021), n.d.

[27] Qian P, Xu Q. Development of Embedded Element Technique for Permeability Analysis of Cracked Porous Media. Math Probl Eng 2017;2017:16–8. doi:10.1155/2017/6713452.

[28] Hamid Sinaei. Evaluation of reinforced concrete beam behaviour using finite element analysis by ABAQUS. Sci Res Essays 2012;7:2002–9. doi:10.5897/SRE11.1393.

[29] Naser MZ, Hawileh RA, Abdalla J. Modeling Strategies of Finite Element Simulation of Reinforced Concrete Beams Strengthened with FRP: A Review. J Compos Sci 2021;5:19. doi:10.3390/jcs5010019.

[30] Tabatabaei SA, Lomov S V., Verpoest I. Assessment of embedded element technique in meso-FE modelling of fibre reinforced composites. Compos Struct 2014;107:436–46. doi:10.1016/j.compstruct.2013.08.020.

[31] Chowdhury NT, Joosten MW, Pearce GMK. An embedded meshing technique (SET) for analysing local strain distributions in textile composites. Compos Struct 2019;210:294–309. doi:10.1016/j.compstruct.2018.11.026.

[32] Harper LT, Qian C, Turner TA, Li S, Warrior NA. Representative volume elements for discontinuous carbon fibre composites - Part 1: Boundary conditions. Compos Sci Technol 2012;72:225–34. doi:10.1016/j.compscitech.2011.11.006.

[33] Lu Z, Yuan Z, Liu Q. 3D numerical simulation for the elastic properties of random fiber composites with a wide range of fiber aspect ratios. Comput Mater Sci 2014;90:123–9. doi:10.1016/j.commatsci.2014.04.007.

[34] Liu H, Zeng D, Li Y, Jiang L. Development of RVE-embedded solid elements model for predicting effective elastic constants of discontinuous fiber reinforced composites. Mech Mater 2016;93:109–23. doi:10.1016/j.mechmat.2015.10.011.

[35] Kabir SMF, Mathur K, Seyam AFM. A critical review on 3D printed continuous fiber-reinforced composites: History, mechanism, materials and properties. Compos Struct 2020;232:111476. doi:10.1016/j.compstruct.2019.111476.

[36] Chacón JM, Caminero MA, Núñez PJ, García-Plaza E, García-Moreno I, Reverte JM. Additive manufacturing of continuous fibre reinforced thermoplastic composites using fused deposition modelling: Effect of process parameters on mechanical properties. Compos Sci Technol 2019;181:107688. doi:10.1016/j.compscitech.2019.107688.

[37]   Der Klift F Van, Koga Y, Todoroki A, Ueda M, Hirano Y, Matsuzaki R. 3D Printing of Continuous Carbon
        Fibre Reinforced Thermo-Plastic (CFRTP) Tensile Test Specimens. Open J Compos Mater 2016;06:18–27.
        doi:10.4236/ojcm.2016.61003.

[38]   Pascual-González C, Iragi M, Fernández A, Fernández-Blázquez JP, Aretxabaleta L, Lopes CS. An approach to
        analyse the factors behind the micromechanical response of 3D-printed composites. Compos Part B Eng
        2020;186:107820. doi:10.1016/j.compositesb.2020.107820.

[39]   Croccolo D, De Agostinis M, Olmi G. Experimental characterization and analytical modelling of the
        mechanical behaviour of fused deposition processed parts made of ABS-M30. Comput Mater Sci 2013;79:506–
        18. doi:10.1016/j.commatsci.2013.06.041.

[40]   Dickson AN, Barry JN, McDonnell KA, Dowling DP. Fabrication of continuous carbon, glass and Kevlar fibre
        reinforced polymer composites using additive manufacturing. Addit Manuf 2017;16:146–52.
        doi:10.1016/j.addma.2017.06.004.

[41]   Polyzos E, Van Hemelrijck D, Pyl L. Numerical modelling of the elastic properties of 3D-printed specimens of
        thermoplastic matrix reinforced with continuous fibres. Compos Part B Eng 2021;211:108671.
        doi:10.1016/J.COMPOSITESB.2021.108671.